

Overpressured underthrust sediment in the Nankai Trough forearc inferred from high-frequency receiver function inversion

Takeshi Akuhara¹, Takeshi Tsuji², and Takashi Tonegawa³

¹Earthquake Research Institute, The University of Tokyo

²Kyushu University

³Japan Agency for Marine-Earth Science and Technology

November 22, 2022

Abstract

Active-source seismic surveys have resolved the fine-scale P-wave velocity (V_p) of the subsurface structure in subduction forearcs. In contrast, the S-wave velocity (V_s) structure is poorly resolved despite its usefulness in understanding rock properties. This study estimates V_p and V_s structures of the Nankai Trough forearc, by applying transdimensional inversion to high-frequency receiver function waveforms. As a result, a thin (~ 1 km) low-velocity zone (LVZ) is evident at ~ 6 km depth beneath the sea level, which locates ~ 3 km seaward from the outer ridge. Based on its high V_p/V_s ratio (~ 2.5) and comparison to an existing seismic reflection profile, we conclude that this LVZ reflects a high pore pressure zone at the upper portion of the underthrust sediment. We infer that this overpressured underthrust sediment hosts slow earthquake activities, and that accompanied strain release helps impede coseismic rupture propagation further updip.

1 **Overpressured underthrust sediment in the Nankai Trough forearc inferred from**
2 **high-frequency receiver function inversion**

3 **Takeshi Akuhara¹, Takeshi Tsuji², and Takashi Tonegawa³**

4 ¹ Earthquake Research Institute, The University of Tokyo

5 ² Department of Earth Resources Engineering, Kyushu University

6 ³ Research Institute for Marine Geodynamics, JAMSTEC

7

8 Corresponding author: Takeshi Akuhara (akuhara@eri.u-tokyo.ac.jp)

9

10 **Key Points:**

- 11 • We applied transdimensional inversion of receiver function waveforms to seafloor cabled
12 stations at the Nankai subduction zone.
- 13 • The resultant high-resolution velocity structures allow a direct comparison to active
14 source surveys.
- 15 • A low-velocity zone beneath the outer ridge is evident, which is interpreted as an
16 overpressured portion of underthrust sediment.

17

18

19 **Abstract**

20 Active-source seismic surveys have resolved the fine-scale P-wave velocity (V_p) of the
21 subsurface structure in subduction forearcs. In contrast, the S-wave velocity (V_s) structure is
22 poorly resolved despite its usefulness in understanding rock properties. This study estimates V_p
23 and V_s structures of the Nankai Trough forearc, by applying transdimensional inversion to high-
24 frequency receiver function waveforms. As a result, a thin (~ 1 km) low-velocity zone (LVZ) is
25 evident at ~ 6 km depth beneath the sea level, which locates ~ 3 km seaward from the outer ridge.
26 Based on its high V_p/V_s ratio (~ 2.5) and comparison to an existing seismic reflection profile, we
27 conclude that this LVZ reflects a high pore pressure zone at the upper portion of the underthrust
28 sediment. We infer that this overpressured underthrust sediment hosts slow earthquake activities,
29 and that accompanied strain release helps impede coseismic rupture propagation further updip.

30 **Plain Language Summary**

31 Many geophysical surveys have investigated the subsurface structures of shallow
32 subduction zones by estimating the propagation speed of compressional waves emitted from
33 artificial explosive sources. Although shear and compressional wave speeds are necessary to
34 understand rock properties (e.g., water content) of the subsurface, it has been difficult to
35 constrain the shear wave speed with a high-resolution. In this study, we estimate both
36 compressional and shear wave speeds by applying an advanced technique to earthquake
37 waveforms recorded at ocean-bottom seismometers deployed at the Nankai subduction zone,
38 Japan. The results show a sufficiently high spatial resolution to detect a thin (~ 1 km) layer,
39 which we interpret as water-rich subducted sediment. This water-rich zone may promote slow
40 slips on the megathrust fault and work as a barrier against rupture propagations during large
41 earthquakes.

43 **1 Introduction**

44 Evaluating the pore fluid pressure distributions in the subduction margins is a key
45 element to understand slip behaviors of the megathrust fault. At accretionary margins,
46 unconsolidated sediment is accreted at the deformation front and further compacted by tectonic
47 loading over time. During this process, abundant fluids are released from the sediment through
48 mechanical compaction or metamorphic dehydration (J. C. Moore & Saffer, 2001). The released
49 fluid can concentrate along nearby faults, and the elevated pore fluid pressure can weaken the
50 fault strength by effectively reducing the normal stress (e.g., Scholz, 1998). Such a weakening
51 mechanism has been suggested to affect the rupture propagation on the megathrust (e.g., Kimura
52 et al., 2012) and contribute to the generation of slow earthquakes (Saffer & Wallace, 2015).

53 Active-source seismic surveys have been widely used to infer pore pressure distribution
54 (e.g., Tsuji, Kamei, et al., 2014). High-resolution (~ 0.1 – 1 km) P-wave velocity (V_p) structure or
55 reflection profiles have been acquired for many subduction zones (Bell et al., 2010; Canales et
56 al., 2017; Gray et al., 2019; Kamei et al., 2012; Li et al., 2015; Shiraishi et al., 2019). In these
57 studies, low V_p or highly reflective zones are often associated with high pore fluid pressure;
58 however, interpreting rock properties from only V_p (or impedance) information is somewhat
59 subjective. With independent estimates of S-wave velocity (V_s), one can acquire more robust
60 constraints on pore fluid pressure (Dvorkin et al., 1999). Unfortunately, marine active-source
61 surveys are not particularly sensitive to V_s .

62 In contrast to active-source surveys, passive-source analyses can be highly sensitive to
63 Vs. The receiver function method (Langston, 1979) aims to retrieve the impulse response of the
64 near-receiver structure, i.e., the Green functions (GFs), from teleseismic P coda by deconvolving
65 incident source wavelet. The retrieved receiver function can then be inverted for the velocity
66 structure beneath the receiver. Early studies used the method at low-frequency (< 1 Hz) to avoid
67 numerical instability of the deconvolution. Later, many studies have improved the technique
68 such that it can work with higher frequencies (e.g., Ligorria & Ammon, 1999), leading to higher
69 spatial resolution (~ 1 km). Nevertheless, most receiver function methods fail to approximate GFs
70 when calculated using data from ocean-bottom seismometers. This is due to intense water
71 reverberations dominating the vertical component records. Recent efforts have overcome this
72 difficulty and allowed for investigating subsurface structure using high-frequency receiver
73 functions with data from offshore observatories (Akuhara et al., 2016, 2017, 2019).

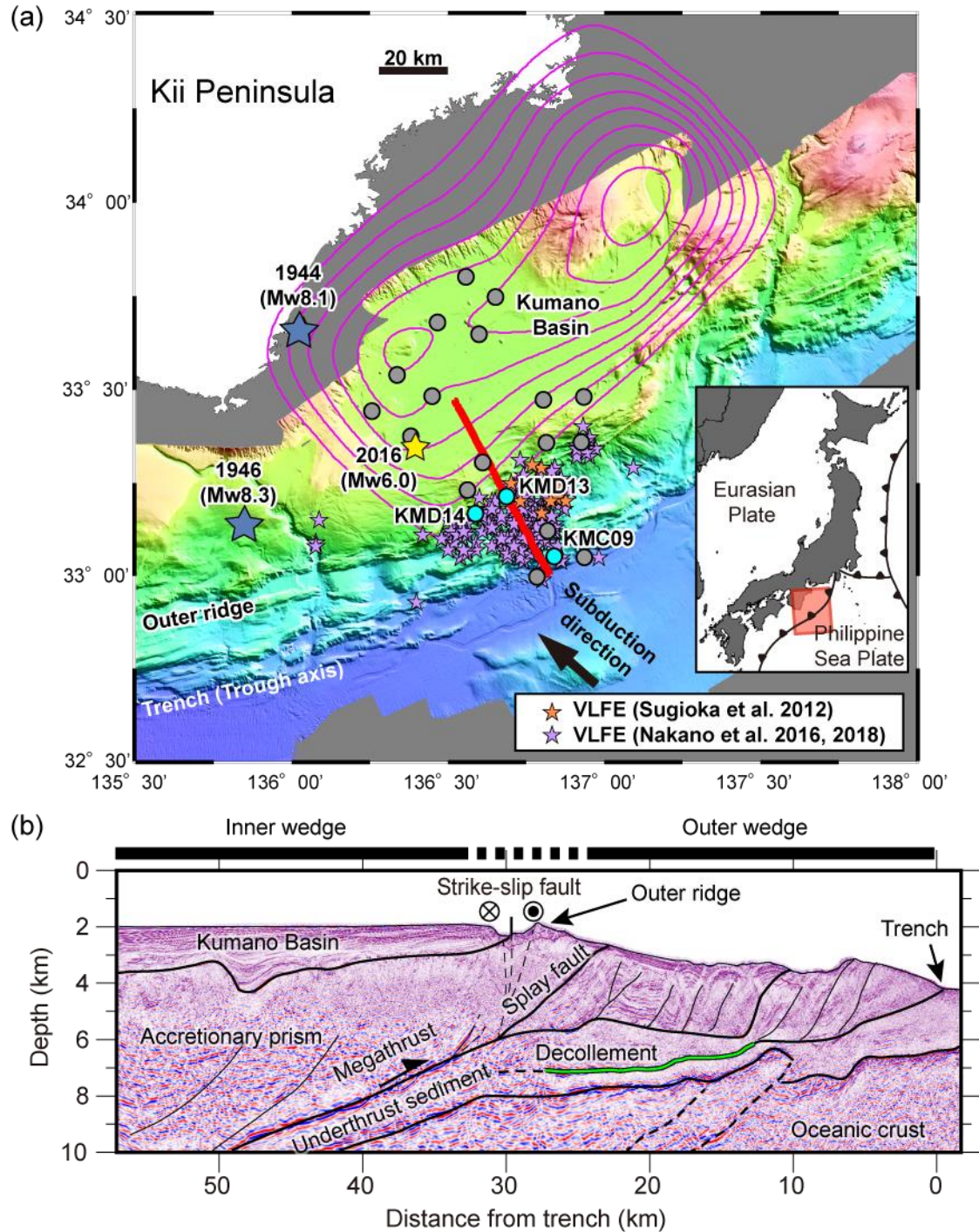
74 This study performs the receiver function inversion for stations from the seafloor cabled
75 network (DONET1) deployed at the Kumano-nada (Kumano Sea) in the central Nankai
76 subduction zone. First, we calculate high-frequency receiver functions, or GFs, using the
77 multichannel deconvolution (MCD) method (Akuhara et al., 2019). Then, the GFs are inverted
78 for the one-dimensional (1-D) seismic velocity structure beneath each station using
79 transdimensional Markov-chain Monte Carlo (MCMC) sampler (Green, 1995). Using this, one
80 can solve an inverse problem without knowing the number of unknowns (i.e., the number of
81 layers in the subsurface structure) a priori. This feature is advantageous for GFs at offshore sites,
82 for which visual interpretation is challenging because of intense reverberatory phases at the sea
83 surface, sea bottom, and sediment-basement interface.

84 The spatial resolution of the resulting velocity structure is sufficiently high to detect a
85 thin (~ 1 km) low-velocity zone (LVZ) that is considered fluid-rich. By comparing the results to
86 the seismic reflection profiles, we detect overpressured features in the Nankai Trough subduction
87 forearc and discuss their implications on the earthquake process. We aim to highlight the
88 advantage of high-resolution studies of Vs structure by receiver functions using offshore data.
89 Future progressive passive-seismic observations at offshore regions can facilitate this class of
90 study, leading to a better understanding of subduction processes.

91

92 **2 Tectonic Setting and Seafloor Observatories**

93 Kumano-nada is in the central Nankai subduction zone, where the Philippine Sea plate
94 obliquely subducts beneath the trough margin (Figure 1a). Megathrust earthquakes repeatedly
95 rupture the plate interface over a cycle of ~ 100 – 150 years (Ando, 1975), including the 1944
96 Tonankai earthquake (Figure 1a, magenta contour). Because of the imminent risk of future
97 megathrust earthquakes, the area's subsurface structure has been intensively investigated by
98 active-source surveys (e.g., Bangs et al., 2009; Kamei et al., 2012; G. F. Moore et al., 2009;
99 Nakanishi et al., 2008; Park et al., 2002). The accretionary prism developed at the margin can be
100 divided into outer and inner wedges. The transition between these two zones is characterized by
101 the outer ridge, splay fault, and strike-slip fault (Figure 1b). All of these features are dominant
102 and thus can be seen along the entire forearc (Tsuji, Ashi, et al., 2014).



103
 104 **Figure 1** (a) Tectonic setting of the study area. Circles denote the seafloor cabled seismometer
 105 network (DONET1). The stations used in this study are colored in sky blue. The bold red line
 106 indicates the location of the seismic reflection profile shown in (b). Orange and purple stars
 107 denote epicenters of very low-frequency earthquakes (Nakano et al., 2016, 2018; Sugioka et al.,
 108 2012). The magenta contour shows coseismic slip distribution during the 1944 Tonankai
 109 Earthquake with an interval of 0.5 m (Kikuchi et al., 2003). (b) Seismic reflection profile
 110 crossing the study area and its interpretation after Tsuji, Kamei, et al. (2014).
 111

112 Despite the progressive surveys, geological interpretation near the plate boundary
 113 remains under debate, even for the shallower portion (i.e., the trenchward side of the outer ridge).
 114 Early works interpreted a strong horizontal reflective surface (Figure 1b, green horizontal line) as
 115 the plate boundary fault (Park et al., 2002), often termed a “décollement”. Later, a three-
 116 dimensional prestack migration study (Park et al., 2010) detected an LVZ ~ 2 km in thickness
 117 immediately above the décollement (Figure S1) and interpreted it as antiformal stacking of the
 118 underthrust sediments. However, the downdip continuation of this LVZ was unclear because of
 119 the limited resolution at depth. Subsequently, full-waveform inversion studies (Kamei et al.,
 120 2012, 2013) have shown that the LVZ extends further downdip to ~ 10 km depth (Figure S1).
 121 Tsuji, Kamei, et al. (2014) interpreted this LVZ as an overpressured shear zone and suggested it
 122 as the location of megathrust faulting. Although the true “thrust” location remains unclear, we
 123 use the term “underthrust” sediment to refer to this LVZ. It should be reminded here that all
 124 studies mentioned above are on the basis of Vp information.

125 The seafloor cable seismometer network, DONET1, has shown a wideband of transient
 126 slips (i.e., slow earthquakes) occurring in this region, including very-low-frequency earthquakes
 127 (VLFES), low-frequency tremors, and slow slip events (Araki et al., 2017; Nakano et al., 2018;
 128 Takemura et al., 2018; To et al., 2015). These epicenters are located updip of the seismically
 129 locked zone where the 1944 Tonankai earthquake ruptured. They have been considered to occur
 130 either on the plate boundary fault or the splay fault within the accretionary prism; this is still an
 131 open question because of the difficulty in obtaining reasonable constraints on their focal depths.
 132 Lines of evidence suggest that the generation of these slow earthquakes is owing to high pore
 133 pressure (Ito & Obara, 2006; Kitajima & Saffer, 2012; Tonegawa et al., 2017).

134 This study mainly focuses on the two DONET1 stations located close to the seismic
 135 reflection profile: one is near the deformation front (KMC09), and the other is near the outer
 136 ridge (KMD13). We additionally use the data from the station KMD14 to highlight the structural
 137 feature obtained near the outer ridge.

138

139 **3 Method**

140 We retrieve the radial component GFs from teleseismic P waveforms using the MCD
 141 technique. This extended receiver function method can be reasonably applied to offshore data
 142 contaminated by intense multiples from the water column (Akuhara et al., 2019). The detailed
 143 processes are as follows. First, we select teleseismic events that occur from November 1st, 2014,
 144 to June 19th, 2019, with $M > 5.5$ and epicentral distances of $30\text{--}90^\circ$. The seismic waveforms of
 145 these are then rotated to the radial-transverse-vertical coordinate system. We measure the signal-
 146 to-noise (SNR) ratio, which we define by the root-mean-square amplitude ratio of 30 s windows
 147 before and after the P arrival, on vertical component records. The records with an $\text{SNR} > 2.5$ are
 148 retained and processed by the MCD. During the deconvolution, a Gaussian low-pass filter
 149 ($G(\omega) = \exp\left(-\frac{\omega^2}{4a^2}\right)$) with a parameter $a=8.0$ is applied. The upper-frequency limit is ~ 3.8 Hz,
 150 at which the filter gain falls to 10% of the maximum. Both radial and vertical component records
 151 are used as inputs to the MCD, which results in GF estimations for both components. In this
 152 study, we only focus on the radial components as the first step.

153 Because of the laterally heterogeneous structure in the study region, resultant GFs vary in
 154 response to incoming ray directions, or event back-azimuths. To avoid this complexity, we

155 divide all GF traces into two subsets (updip or downdip datasets) depending on the incoming
 156 direction relative to the subducting plate. For each subset, we calculate cross-correlation
 157 coefficients (CCs) between all pairs of GFs and select GFs that show high coherency ($CC > 0.65$)
 158 with at least half of all GFs within the subset (Figure S2). GFs satisfying this condition are
 159 stacked and used as input data for the following inversion analysis. We carry out the inversion
 160 analysis separately for each updip and downdip data, leading to two independent results per
 161 station.

162 We employ transdimensional MCMC inversion (e.g., Agostinetti & Malinverno, 2010;
 163 Bodin et al., 2012) for solving seismic velocity structures. We assume an isotropic layered
 164 medium beneath the seafloor (i.e., the station level) and express the structure using the following
 165 unknowns: the number of layer interfaces (k), their depths ($z_i, i = 1 \dots k$), and the P and S-wave
 166 velocity anomalies ($\delta\alpha_i$ and $\delta\beta_i, i = 1 \dots k + 1$). These velocity anomalies are defined relative
 167 to the station-specific reference velocity models estimated by Tonegawa et al. (2017). These
 168 velocity models are determined from Rayleigh wave admittance, a ratio of the vertical
 169 displacement to the pressure on the seafloor (Ruan et al., 2014), offering a reasonable constraint
 170 on Vs. The densities are scaled to Vp by an empirical relation (Brocher, 2005). The properties of
 171 the ocean layer are fixed as follows: Vp and density are assumed to be 1.5 km/s and 1.0 g/cm³,
 172 respectively, and the station level is used for the thickness. Although there are some reports of
 173 anisotropy in the study region (Tsuji et al., 2011), we limit our analysis to the isotropic case for
 174 simplicity.

175 The posterior probability in terms of $k, z_i, \delta\alpha_i,$ and $\delta\beta_i$, which is proportional to the
 176 prior-likelihood product, is sampled by the reversible-jump MCMC algorithm (Green, 1995).
 177 The method explores multidimensional model space via random walks (i.e., perturbing $z_i, \delta\alpha_i,$
 178 and $\delta\beta_i$), together with the random increase/decrease in the model space dimension (i.e.,
 179 increasing/decreasing k). We assume truncated uniform priors for k and z_i and zero-mean
 180 Gaussian priors for $\delta\alpha_i$ and $\delta\beta_i$. Besides these priors, we prohibit anomalous layers with either
 181 too high/low velocities or Vp/Vs. We employ the propagator matrix method (Thomson, 1950)
 182 for the forward computation, and then the likelihood is calculated in the manner that can consider
 183 a temporal correlation of data noise (Bodin et al., 2012). A parallel tempering method
 184 (Sambridge, 2014) is adopted to increase the conversion rate of the inversion. See Text S1 for
 185 more details of the MCMC inversion.

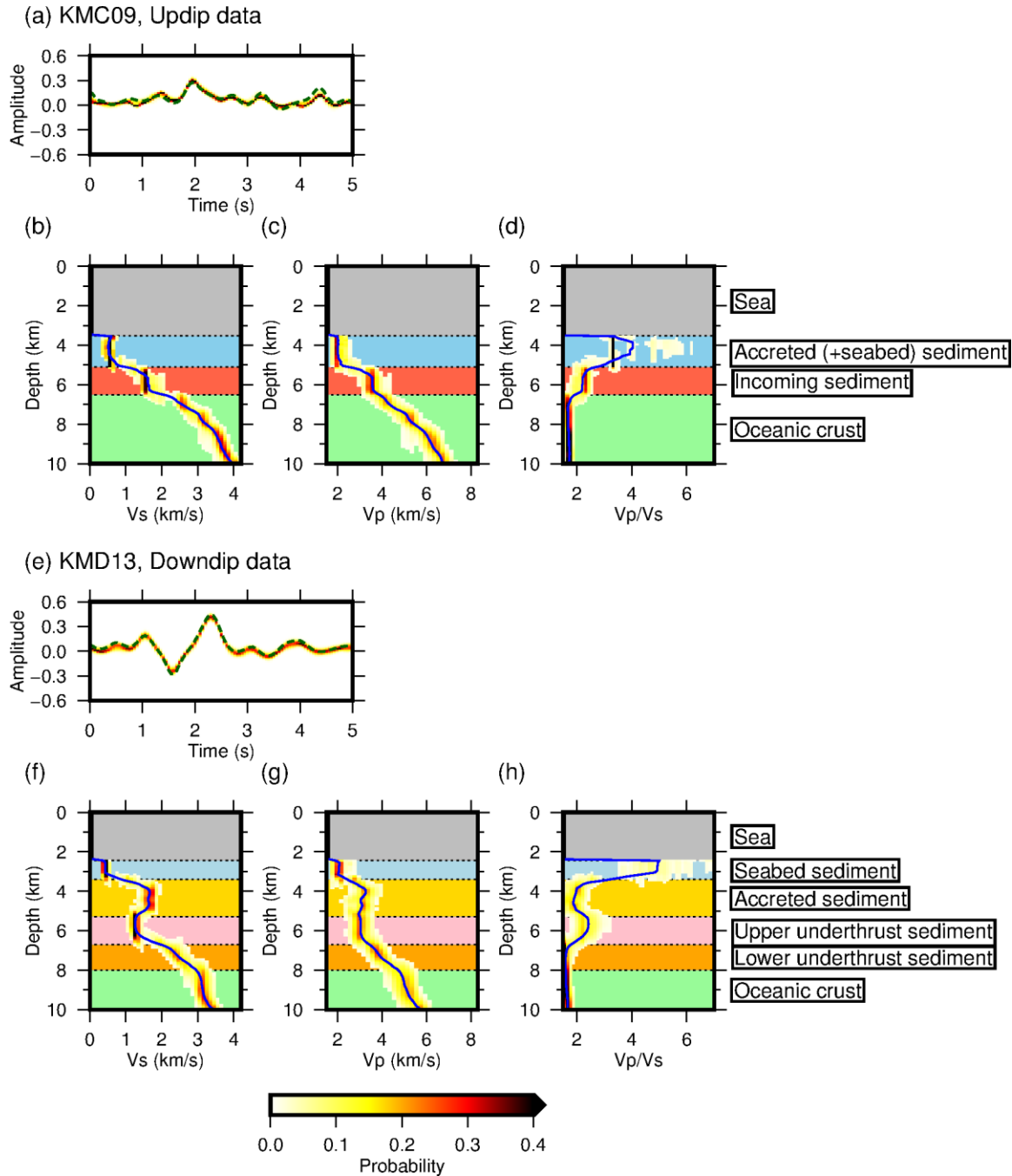
186 The models sampled by the MCMC construct the posterior probability distribution, from
 187 which any derivatives, including marginal probability, mean model, or confidence interval, can
 188 be drawn. Recall that we obtain two independent probability distributions per station derived
 189 from the updip and downdip datasets. Comparing these results may provide useful insight into
 190 lateral heterogeneity. In our results, however, the difference is found to be negligible, with an
 191 exception discussed later. In the following section, we report confidence intervals of Vs and
 192 Vp/Vs that are calculated by simply merging the two results.

193

194 **4 Results and Interpretations**

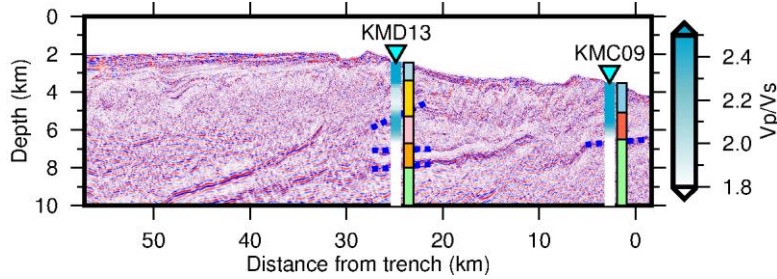
195 The inverted velocity structure for the site close to the trench (KMC09) shows two thin
 196 (< 2 km) layers immediately beneath the seafloor (Figures 2a-d, S3). The 95% confidence
 197 intervals of Vs and Vp/Vs for the upper layer are 0.5–0.8 km/s and 3.2–4.3, respectively, while

198 the lower layer exhibits 0.9–1.8 km/s and 1.8–3.4. Comparing to the seismic reflection profile,
199 we interpret these layers as the incoming sediment overlaid by the accreted sediment (Figure 3).
200 The extremely low V_s and high V_p/V_s indicate the unconsolidated nature of the sediment. Such
201 a high V_p/V_s of the sediment near the deformation front is also inferred from a refraction survey
202 using converted phases (Tsuji et al., 2011). The sharp drop in V_p/V_s to < 2.0 at 6.5 km depth
203 well defines the sediment-oceanic crust interface and closely matches the reflective band seen in
204 the profile of Figure 3. V_s at the top of the oceanic crust is estimated to be ~ 2.5 km/s, which is
205 expected for the basaltic layer known as oceanic layer 2 (Christensen, 1978). The velocity
206 gradually increases with depth to ~ 4.8 km/s at 10 km depth, considered as the gabbroic oceanic
207 crust (oceanic layer 3).



208
209
210
211
212
213
214

Figure 2 Results of inversion analysis for (a-d) KMC09 and (e-h) KMD13. (a, e) Input Green's functions (green dashed line) and the frequency distribution of predicted Green's functions (red and yellow gradation). (b-d, f-h) Posterior marginal probability distributions of (b, f) V_s , (c, g), V_p , and (d, h) V_p/V_s structures (red and yellow gradation). Note that negligible probability (< 0.01) is muted. The blue lines represent the mean models. The background color shows the geological interpretation.



215 **Figure 3** Comparison of V_p/V_s to the seismic reflection profile. The bluish color shows V_p/V_s
 216 (i.e., the mean model) estimated by this study. Colored rectangles indicate the geological
 217 interpretation with the same color notation as Figure 2. The blue dotted line segments highlight
 218 reflective bands that agree with our interpretation.
 219
 220

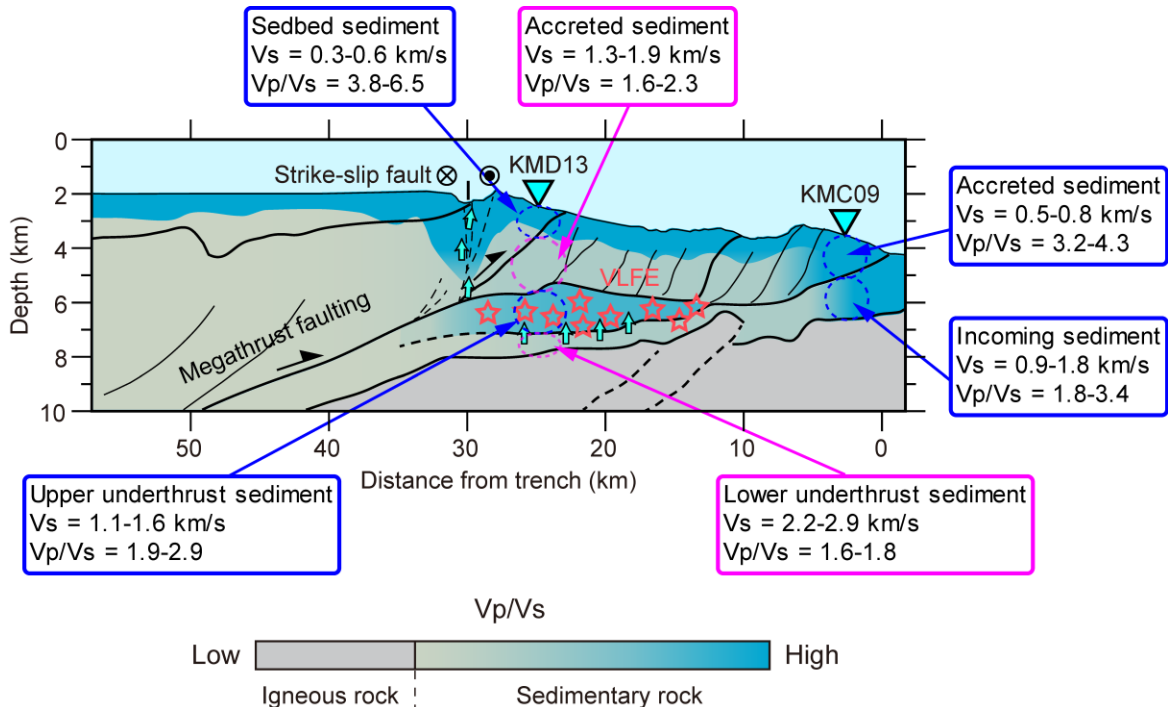
221 The inverted velocity structure near the outer ridge (KMD13) can be divided into five
 222 geological units: the seedbed sediment, accreted sediment, upper underthrust sediment, lower
 223 underthrust sediment, and oceanic crust (Figures 2e-h and S4). Note that we define these
 224 boundaries by discontinuities in V_s or V_p/V_s , but they are mostly consistent with the reflective
 225 band seen in the reflection profile (Figure 3). Remarkably, the upper underthrust sediment
 226 exhibits lower V_s (with a 95% confidence interval of 1.1–1.6 km/s) and higher V_p/V_s (1.9–2.9)
 227 than above it. The stratification of marine sediments typically shows the highest V_p/V_s at its top,
 228 and the ratio decreases with depth because of the increase in effective stress (e.g., Hamilton,
 229 1979). The higher V_p/V_s than that of the shallower part, as seen here, can be explained by
 230 elevated pore pressure (Dvorkin et al., 1999). Note that the low V_s obtained is essential here
 231 because the low V_p can be explained by gas saturation in addition to high pore pressure. The
 232 lower underthrust sediment shows distinguishably higher V_s (or lower V_p/V_s) compared to the
 233 upper underthrust sediment. The sharp V_s contrast is most likely to correspond to the
 234 décollement interpreted on the reflection profile (Figures 1b and 3). We, therefore, conclude that
 235 fluid is confined in the volume between the décollement and the base of accreted sediment.

236 We notice that the low-velocity feature for the upper underthrust sediment is not clear in
 237 the results from the updip data (Figure S4). This may be due to the effect of a dipping layer. The
 238 incident angle to the dipping layer is smaller for ray paths from the updip direction, leading to
 239 less efficient P-to-S conversions at the interface. Indeed, the top-surface of the underthrust
 240 sediment indicates a steeper dip angle than the décollement and the top of the oceanic crust
 241 (Figure 3). Reasonable treatment for this dipping effect will improve the V_s estimation for this
 242 layer, which is left for our future work. Additional inversion analysis on KMD14, which locates
 243 in a similar tectonic setting, provides another supportive evidence. The result shows a similar
 244 pattern to KMD13 in that it consists of the same five geological units with comparable velocities
 245 (Figure S5).

247 5 Discussion and Conclusions

248 We estimated 1-D seismic velocity (V_p and V_s) structures beneath the DONET1 stations,
 249 located in the center of the Nankai subduction zone, using transdimensional MCMC inversion.
 250 The high-frequency content (up to ~ 3.8 Hz) of the input waveforms offers a high spatial
 251 resolution sufficient for a direct comparison to the seismic reflection profile. Regarding a high
 252 V_p/V_s as an indicator of high pore pressure, we detected fluid-rich features in the forearc margin

253 (Figure 4). At the onset of the subduction (KMC09), both incoming and accreted sediments
 254 indicate the mean V_p/V_s higher than 2, indicative of the unconsolidated nature. Near the outer
 255 ridge (KMD13), V_p/V_s of the accreted sediment is relatively low. We consider that this decrease
 256 in V_p/V_s reflects consolidation because of mechanical compaction under tectonic loading.



257 **Figure 4** Schematic illustration of our interpretations. The background color indicates the
 258 interpolation and extrapolation of V_p/V_s obtained in this study. The 95% confidence intervals of
 259 V_s and V_p/V_s are shown for each geological unit. The orange stars represent very-low-frequency
 260 earthquakes. The sky-blue arrows depict fluid flow.
 261

262 A remarkable finding is the LVZ within the upper portion of the underthrust sediment.
 263 Although a similar LVZ has been previously reported based on V_p information (Kamei et al.,
 264 2013; Park et al., 2010; see Figure S1), our results clarify that the overpressured zone (i.e., the
 265 high V_p/V_s zone) localizes within only the upper portion of the underthrust sediment, right
 266 above the décollement. This zone between the décollement and the base of accreted sediment
 267 was interpreted as shear zone in previous study (Tsuji, Kamei et al., 2014). Fluids may be
 268 trapped in this portion with the aid of the permeability barrier by compacted but still well
 269 stratified accretionary sediment above. In contrast, the lower underthrust thrust sediment is
 270 considered dewatered in light of its relatively high V_s and low V_p/V_s . Mechanical compaction
 271 and metamorphic dehydration (J. C. Moore & Saffer, 2001) may squeeze fluid from the lower
 272 underthrust sediment, and the fluid may ascend to the upper part, contributing to the fluid-rich
 273 condition.

274 The LVZ in the underthrust sediment invokes the widely accepted idea that slow
 275 earthquakes, including VLFEs, occur where pore fluid pressure is high (Saffer & Wallace, 2015).
 276 Following this notion, we consider that VLFEs in this region most likely to occur within the
 277 upper portion of the underthrust sediment, where we infer high pore pressure. Notably, the VLFE
 278 region bounds on the 1944 Tonankai earthquake's rupture zone (Figure 1a). Strain release by the
 279 intense VLFE activities may impede the coseismic rupture propagation further updip into the

280 VLFE region. Instead, the rupture may propagate along the splay fault (Baba et al., 2006).
 281 Furthermore, the fluid-rich underthrust sediment beneath the outer ridge may weaken the
 282 strength of the hanging wall such that strike-slip motion along the outer ridge (Tsuji, Ashi, et al.,
 283 2014) can occur (Figure 4). The Vp model of Kamei et al. (2013) supports this idea in that it
 284 predicts a low Vp zone near the strike-slip fault. The strain partitioning due to this strike-slip
 285 motion could be another key factor that impedes the rupture propagation.

286 This study shows the possibility of receiver function analysis as a new tool to study fluid-
 287 related heterogeneities in subduction forearcs; our method can provide unique constraints on Vs
 288 (or Vp/Vs) with a comparable resolution to that of active-source surveys. Seismometer
 289 instrumentation on the seafloor has become popular worldwide. Future applications of our
 290 method to such offshore seismometer networks (or more dense deployments in the near future)
 291 await.

292 **Acknowledgment**

293 We thank Rie Nakata (Kamei) for providing the velocity model. This study was
 294 supported by JSPS KAKENHI Grant Numbers JP16H06472, JP16H06475, JP19K14811, and
 295 JP19K21892. Waveform data of DONET1 stations are available on the web page of National
 296 Research Institute for Earth Science and Disaster Resilience
 297 (<https://doi.org/10.17598/nied.0008>). The computer programs of MCD and MCMC inversion are
 298 available at the Zenodo web page (<https://doi.org/10.5281/zenodo.2548974>, and
 299 <https://doi.org/10.5281/zenodo.3663089>, respectively). Hypocenters of VLFs were downloaded
 300 from Slow Earthquake Database (Kano et al., 2018; [http://www-solid.eps.s.u-](http://www-solid.eps.s.u-tokyo.ac.jp/~sloweq)
 301 [tokyo.ac.jp/~sloweq](http://www-solid.eps.s.u-tokyo.ac.jp/~sloweq)).

302

303 **References**

- 304 Agostinetti, N. P., & Malinverno, A. (2010). Receiver function inversion by trans-dimensional
 305 Monte Carlo sampling. *Geophysical Journal International*, *181*(2), 858–872.
 306 <https://doi.org/10.1111/j.1365-246X.2010.04530.x>
- 307 Akuhara, T., Mochizuki, K., Kawakatsu, H., & Takeuchi, N. (2016). Non-linear waveform
 308 analysis for water-layer response and its application to high-frequency receiver function
 309 analysis using OBS array. *Geophysical Journal International*, *206*(3), 1914–1920.
 310 <https://doi.org/10.1093/gji/ggw253>
- 311 Akuhara, T., Mochizuki, K., Kawakatsu, H., & Takeuchi, N. (2017). A fluid-rich layer along the
 312 Nankai trough megathrust fault off the Kii Peninsula inferred from receiver function
 313 inversion. *Journal of Geophysical Research: Solid Earth*, *122*(8), 6524–6537.
 314 <https://doi.org/10.1002/2017JB013965>
- 315 Akuhara, T., Bostock, M. G., Plourde, A. P., & Shinohara, M. (2019). Beyond Receiver
 316 Functions: Green's Function Estimation by Transdimensional Inversion and Its Application
 317 to OBS Data. *Journal of Geophysical Research: Solid Earth*, *124*(2), 1944–1961.
 318 <https://doi.org/10.1029/2018JB016499>

- 319 Ando, M. (1975). Source mechanisms and tectonic significance of historical earthquakes along
320 the Nankai trough, Japan. *Tectonophysics*, 27(2), 119–140. <https://doi.org/10.1016/0040->
321 1951(75)90102-X
- 322 Araki, E., Saffer, D. M., Kopf, A. J., Wallace, L. M., Kimura, T., Machida, Y., et al. (2017).
323 Recurring and triggered slow-slip events near the trench at the Nankai Trough subduction
324 megathrust. *Science*. <https://doi.org/10.1126/science.aan3120>
- 325 Baba, T., Cummins, P. R., Hori, T., & Kaneda, Y. (2006). High precision slip distribution of the
326 1944 Tonankai earthquake inferred from tsunami waveforms: Possible slip on a splay fault.
327 *Tectonophysics*, 426(1–2), 119–134. <https://doi.org/10.1016/j.tecto.2006.02.015>
- 328 Bangs, N. L. B., Moore, G. F., Gulick, S. P. S., Pangborn, E. M., Tobin, H. J., Kuramoto, S., &
329 Taira, A. (2009). Broad, weak regions of the Nankai Megathrust and implications for
330 shallow coseismic slip. *Earth and Planetary Science Letters*, 284(1–2), 44–49.
331 <https://doi.org/10.1016/j.epsl.2009.04.026>
- 332 Bell, R., Sutherland, R., Barker, D. H. N., Henrys, S., Bannister, S., Wallace, L., & Beavan, J.
333 (2010). Seismic reflection character of the Hikurangi subduction interface, New Zealand, in
334 the region of repeated Gisborne slow slip events. *Geophysical Journal International*,
335 180(1), 34–48. <https://doi.org/10.1111/j.1365-246X.2009.04401.x>
- 336 Bodin, T., Sambridge, M., Tkalčić, H., Arroucau, P., Gallagher, K., & Rawlinson, N. (2012).
337 Transdimensional inversion of receiver functions and surface wave dispersion. *Journal of*
338 *Geophysical Research: Solid Earth*, 117(2), 1–24. <https://doi.org/10.1029/2011JB008560>
- 339 Brocher, T. M. (2005). Empirical relations between elastic wavespeeds and density in the Earth's
340 crust. *Bulletin of the Seismological Society of America*, 95(6), 2081–2092.
341 <https://doi.org/10.1785/0120050077>
- 342 Canales, J. P., Carbotte, S. M., Nedimovic, M. R., & Carton, H. (2017). Dry Juan de Fuca slab
343 revealed by quantification of water entering Cascadia subduction zone. *Nature Geoscience*.
344 <https://doi.org/10.1038/NGEO3050>
- 345 Christensen, I. (1978). Ophiolites, structure seismic velocities and oceanic crustal. *Program*, 47,
346 131–157.
- 347 Dvorkin, J., Mavko, G., & Nur, A. (1999). Overpressure detection from compressional- and
348 shear-wave data. *Geophysical Research Letters*. <https://doi.org/10.1029/1999GL008382>
- 349 Gray, M., Bell, R. E., Morgan, J. V., Henrys, S., & Barker, D. H. N. (2019). Imaging the Shallow
350 Subsurface Structure of the North Hikurangi Subduction Zone, New Zealand, Using 2-D
351 Full-Waveform Inversion. *Journal of Geophysical Research: Solid Earth*.
352 <https://doi.org/10.1029/2019JB017793>
- 353 Green, P. J. (1995). Reversible jump Markov chain monte carlo computation and Bayesian
354 model determination. *Biometrika*, 82(4), 711–732. <https://doi.org/10.1093/biomet/82.4.711>
- 355 Hamilton, E. L. (1979). V_p / V_s and Poisson's ratios in marine sediments and rocks. *The*
356 *Journal of the Acoustical Society of America*, 66(4), 1093–1101.
357 <https://doi.org/10.1121/1.383344>

- 358 Ito, Y., & Obara, K. (2006). Very low frequency earthquakes within accretionary prisms are very
359 low stress-drop earthquakes. *Geophysical Research Letters*.
360 <https://doi.org/10.1029/2006GL025883>
- 361 Kamei, R., Pratt, R. G., & Tsuji, T. (2012). Waveform tomography imaging of a megasplay fault
362 system in the seismogenic Nankai subduction zone. *Earth and Planetary Science Letters*,
363 317–318, 343–353. <https://doi.org/10.1016/j.epsl.2011.10.042>
- 364 Kamei, R., Pratt, R. G., & Tsuji, T. (2013). On acoustic waveform tomography of wide-angle
365 OBS data-strategies for pre-conditioning and inversion. *Geophysical Journal International*,
366 194(2), 1250–1280. <https://doi.org/10.1093/gji/ggt165>
- 367 Kikuchi, M., Nakamura, M., & Yoshikawa, K. (2003). Source rupture processes of the 1944
368 Tonankai earthquake and the 1945 Mikawa earthquake derived from low-gain seismograms.
369 *Earth, Planets and Space*. <https://doi.org/10.1186/BF03351745>
- 370 Kimura, G., Hina, S., Hamada, Y., Kameda, J., Tsuji, T., Kinoshita, M., & Yamaguchi, A.
371 (2012). Runaway slip to the trench due to rupture of highly pressurized megathrust beneath
372 the middle trench slope: The tsunamigenesis of the 2011 Tohoku earthquake off the east
373 coast of northern Japan. *Earth and Planetary Science Letters*, 339–340, 32–45.
374 <https://doi.org/10.1016/j.epsl.2012.04.002>
- 375 Kitajima, H., & Saffer, D. M. (2012). Elevated pore pressure and anomalously low stress in
376 regions of low frequency earthquakes along the Nankai Trough subduction megathrust.
377 *Geophysical Research Letters*. <https://doi.org/10.1029/2012GL053793>
- 378 Langston, C. A. (1979). Structure under Mount Rainier, Washington, inferred from teleseismic
379 body waves. *Journal of Geophysical Research*, 84(B9), 4749–4762.
380 <https://doi.org/10.1029/JB084iB09p04749>
- 381 Li, J., Shillington, D. J., Bécel, A., Nedimović, M. R., Webb, S. C., Saffer, D. M., et al. (2015).
382 Downdip variations in seismic reflection character: Implications for fault structure and
383 seismogenic behavior in the Alaska subduction zone. *Journal of Geophysical Research:*
384 *Solid Earth*. <https://doi.org/10.1002/2015JB012338>
- 385 Ligorria, J. P., & Ammon, C. J. (1999). Iterative deconvolution and receiver-function estimation.
386 *Bulletin of the Seismological Society of America*, 89(5), 1395–1400.
- 387 Moore, G. F., Park, J.-O., Bangs, N. L., Gulick, S. P., Tobin, H. J., Nakamura, Y., et al. (2009).
388 Structural and seismic stratigraphic framework of the NanTroSEIZE Stage 1 transect, 314.
389 <https://doi.org/10.2204/iodp.proc.314315316.102.2009>
- 390 Moore, J. C., & Saffer, D. (2001). Updip limit of the seismogenic zone beneath the accretionary
391 prism of Southwest Japan: An effect of diagenetic to low-grade metamorphic processes and
392 increasing effective stress. *Geology*. [https://doi.org/10.1130/0091-](https://doi.org/10.1130/0091-7613(2001)029<0183:ULOTSZ>2.0.CO;2)
393 [7613\(2001\)029<0183:ULOTSZ>2.0.CO;2](https://doi.org/10.1130/0091-7613(2001)029<0183:ULOTSZ>2.0.CO;2)
- 394 Nakanishi, A., Kodaira, S., Miura, S., Ito, A., Sato, T., Park, J. O., et al. (2008). Detailed
395 structural image around splay-fault branching in the Nankai subduction seismogenic zone:
396 Results from a high-density ocean bottom seismic survey. *Journal of Geophysical*
397 *Research: Solid Earth*, 113(3), 1–14. <https://doi.org/10.1029/2007JB004974>

- 398 Nakano, M., Hori, T., Araki, E., Takahashi, N., & Kodaira, S. (2016). Ocean Floor Networks
399 Capture Low-Frequency Earthquake Event. *Eos*, 97. <https://doi.org/10.1029/2016EO052877>
- 400 Nakano, M., Hori, T., Araki, E., Kodaira, S., & Ide, S. (2018). Shallow very-low-frequency
401 earthquakes accompany slow slip events in the Nankai subduction zone. *Nature*
402 *Communications*, 9(1), 984. <https://doi.org/10.1038/s41467-018-03431-5>
- 403 Park, J. O., Tsuru, T., Kodaira, S., Cummins, P. R., & Kaneda, Y. (2002). Splay fault branching
404 along the Nankai subduction zone. *Science*, 297(5584), 1157–1160.
405 <https://doi.org/10.1126/science.1074111>
- 406 Park, J. O., Fujie, G., Wijerathne, L., Hori, T., Kodaira, S., Fukao, Y., et al. (2010). A low-
407 velocity zone with weak reflectivity along the Nankai subduction zone. *Geology*, 38(3),
408 283–286. <https://doi.org/10.1130/G30205.1>
- 409 Ruan, Y., Forsyth, D. W., & Bell, S. W. (2014). Marine sediment shear velocity structure from
410 the ratio of displacement to pressure of Rayleigh waves at seafloor. *Journal of Geophysical*
411 *Research: Solid Earth*. <https://doi.org/10.1002/2014JB011162>
- 412 Saffer, D. M., & Wallace, L. M. (2015). The frictional, hydrologic, metamorphic and thermal
413 habitat of shallow slow earthquakes. *Nature Geoscience*, 8(8), 594–600.
414 <https://doi.org/10.1038/ngeo2490>
- 415 Sambridge, M. (2014). A Parallel Tempering algorithm for probabilistic sampling and
416 multimodal optimization. *Geophysical Journal International*, 196(1), 357–374.
417 <https://doi.org/10.1093/gji/ggt342>
- 418 Scholz, C. H. (1998). Earthquakes and friction laws. *Nature*, 391(6662), 37–42.
419 <https://doi.org/10.1038/34097>
- 420 Shiraishi, K., Moore, G. F., Yamada, Y., Kinoshita, M., Sanada, Y., & Kimura, G. (2019).
421 Seismogenic Zone Structures Revealed by Improved 3-D Seismic Images in the Nankai
422 Trough off Kumano. *Geochemistry, Geophysics, Geosystems*, 20(5), 2252–2271.
423 <https://doi.org/10.1029/2018GC008173>
- 424 Sugioka, H., Okamoto, T., Nakamura, T., Ishihara, Y., Ito, A., Obana, K., et al. (2012).
425 Tsunamigenic potential of the shallow subduction plate boundary inferred from slow
426 seismic slip. *Nature Geoscience*, 5(6), 414–418. <https://doi.org/10.1038/ngeo1466>
- 427 Takemura, S., Matsuzawa, T., Kimura, T., Tonegawa, T., & Shiomi, K. (2018). Centroid
428 Moment Tensor Inversion of Shallow Very Low Frequency Earthquakes Off the Kii
429 Peninsula, Japan, Using a Three-Dimensional Velocity Structure Model. *Geophysical*
430 *Research Letters*. <https://doi.org/10.1029/2018GL078455>
- 431 Thomson, W. T. (1950). Transmission of elastic waves through a stratified medium. *Journal of*
432 *Applied Physics*, 21(1950), 89–93; 89.
- 433 To, A., Obana, K., Sugioka, H., Araki, E., Takahashi, N., & Fukao, Y. (2015). Small size very
434 low frequency earthquakes in the Nankai accretionary prism, following the 2011 Tohoku-
435 Oki earthquake. *Physics of the Earth and Planetary Interiors*.
436 <https://doi.org/10.1016/j.pepi.2015.04.007>

- 437 Tonegawa, T., Araki, E., Kimura, T., Nakamura, T., Nakano, M., & Suzuki, K. (2017). Sporadic
438 low-velocity volumes spatially correlate with shallow very low frequency earthquake
439 clusters. *Nature Comm.*, 8(2048), 1–7. <https://doi.org/10.1038/s41467-017-02276-8>
- 440 Tsuji, T., Dvorkin, J., Mavko, G., Nakata, N., Matsuoka, T., Nakanishi, A., et al. (2011). V P / V
441 S ratio and shear-wave splitting in the Nankai Trough seismogenic zone: Insights into
442 effective stress, pore pressure, and sediment consolidation. *Geophysics*, 76(3), WA71-
443 WA82. <https://doi.org/10.1190/1.3560018>
- 444 Tsuji, T., Kamei, R., & Pratt, R. G. (2014). Pore pressure distribution of a mega-splay fault
445 system in the Nankai trough subduction zone: Insight into up-dip extent of the seismogenic
446 zone. *Earth and Planetary Science Letters*, 396, 165–178.
447 <https://doi.org/10.1016/j.epsl.2014.04.011>
- 448 Tsuji, T., Ashi, J., & Ikeda, Y. (2014). Strike-slip motion of a mega-splay fault system in the
449 Nankai oblique subduction zone. *Earth, Planets and Space*, 66(1), 120.
450 <https://doi.org/10.1186/1880-5981-66-120>
- 451

1

2

Geophysical Research Letters

3

Supporting Information for

4

Overpressured underthrust sediment in the Nankai Trough forearc inferred from high-frequency receiver function inversion

5

6

Takeshi Akuhara¹, Takeshi Tsuji², and Takashi Tonegawa³

7

¹Earthquake Research Institute, The University of Tokyo, ²Department of Earth Resources Engineering, Kyushu University, ³Research Institute for Marine Geodynamics, JAMSTEC

8

9

10

Contents of this file

11

12

Text S1

13

Figures S1 to S5

14

Tables S1 to S2

15

16

Introduction

17

This supporting information provides: details of the transdimensional Markov-chain Monte Carlo inversion (Text S1); P-wave velocity models by previous studies (Figures S1); procedure of Green's function selection (Figure S2); inversion results that are not shown in the main text (Figures S3–5); and lists of tuning parameters for the inversion analysis (Tables S1–2).

20

21

22 **Text S1. Transdimensional Markov-chain Monte Carlo inversion**

23 The transdimensional Markov-chain Monte Carlo (MCMC) inversion estimates the posterior
 24 probability of k and $\mathbf{m}_k = (z_1 \cdots z_k, \delta\alpha_1 \cdots \delta\alpha_{k+1}, \delta\beta_1 \cdots \delta\beta_{k+1})^T$ with the given input data, \mathbf{d} ,
 25 as follows:

$$\begin{aligned} P(k, \mathbf{m}_k | \mathbf{d}) &\propto P(k)P(\mathbf{m}_k | k)P(\mathbf{d} | k, \mathbf{m}_k) \\ &= P(k) \prod_{i=1}^k \{P(z_i)\} \prod_{i=1}^{k+1} \{P(\delta\alpha_i)\} \prod_{i=1}^{k+1} \{P(\delta\beta_i)\} P(\mathbf{d} | k, \mathbf{m}_k), \#(S1) \end{aligned}$$

26 where $P(x|y)$ represents the probability to realize x with y given, and $P(x)$ is a prior
 27 probability of x . The other notations are defined in Section 3 of the main text.

28 As the prior probabilities for k and z_i , we assume truncated uniform priors bounded from
 29 k_{min} to k_{max} and from z_{min} to z_{max} , respectively:

$$P(k) = \begin{cases} \frac{1}{k_{max} - k_{min}} & (k_{min} \leq k < k_{max}) \\ 0 & (\text{otherwise}) \end{cases} \#(S2)$$

30 and

$$P(z_i) = \begin{cases} \frac{1}{z_{max} - z_{min}} & (z_{min} \leq z_i \leq z_{max}) \\ 0 & (\text{otherwise}) \end{cases} \#(S3)$$

31 For the velocity anomalies, we assume Gaussian priors with zero-mean and standard
 32 deviations of $\sigma_{\delta\alpha}$ and $\sigma_{\delta\beta}$ as follows:

$$P(\delta\alpha_i) = \frac{1}{\sqrt{2\pi\sigma_{\delta\alpha}^2}} \exp\left(-\frac{\delta\alpha_i^2}{2\sigma_{\delta\alpha}^2}\right), \#(S4)$$

33 and

$$P(\delta\beta_i) = \frac{1}{\sqrt{2\pi\sigma_{\delta\beta}^2}} \exp\left(-\frac{\delta\beta_i^2}{2\sigma_{\delta\beta}^2}\right). \#(S5)$$

34 Here, k_{min} , k_{max} , z_{min} , z_{max} , $\sigma_{\delta\alpha}$, and $\sigma_{\delta\beta}$ are parameters selected in accordance with prior
 35 knowledge. The values used in this study are summarized in Table S1.

36 With a given model, \mathbf{m}_k , synthetic GF, $\mathbf{g}(k, \mathbf{m}_k)$, is computed using the propagator matrix
 37 method (Thomson, 1950). Then, the likelihood, $P(\mathbf{d} | k, \mathbf{m}_k)$, can be calculated as follows:

$$P(\mathbf{d}|k, \mathbf{m}_k) = \frac{1}{\sqrt{(2\pi)^N |\mathbf{C}|}} \exp \left[-\frac{1}{2} \{\mathbf{g}(k, \mathbf{m}_k) - \mathbf{d}\}^T \mathbf{C}^{-1} \{\mathbf{g}(k, \mathbf{m}_k) - \mathbf{d}\} \right], \#(S6)$$

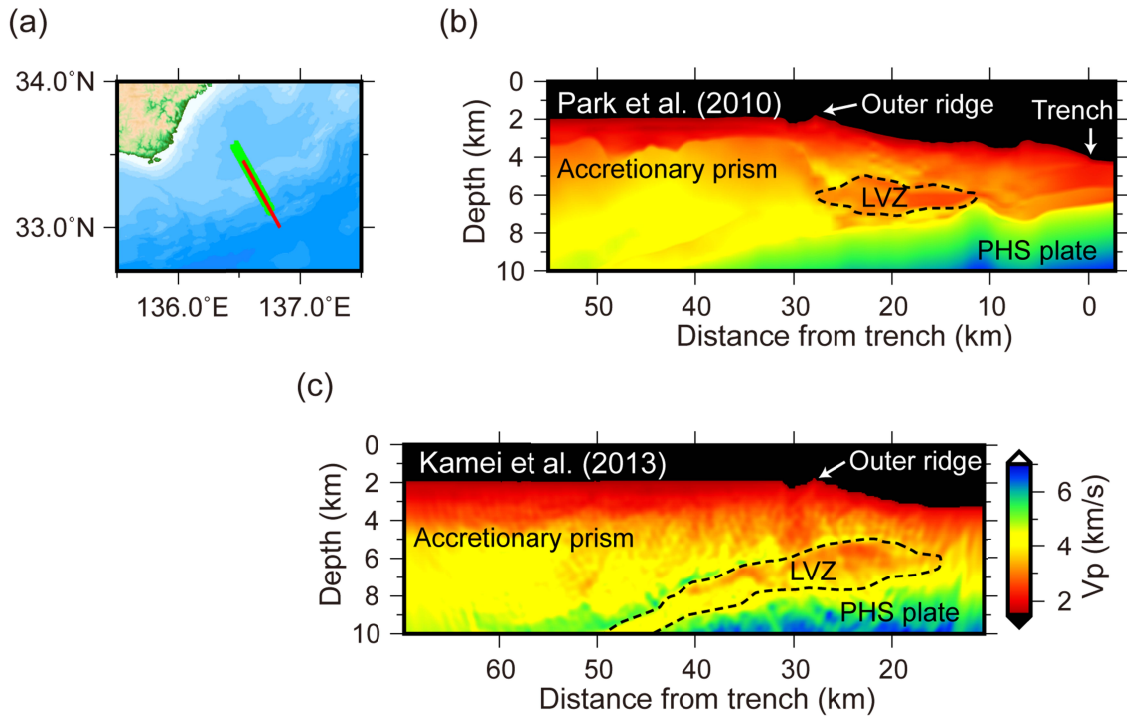
38 where \mathbf{C} is the covariance matrix, and N is the number of elements in the time series.
 39 Following Bodin et al. (2012), we parameterize the covariance matrix by $C_{ij} = \sigma^2 r^{(j-i)^2}$, in
 40 which σ denotes a standard deviation of data noise, and r denotes the noise temporal
 41 correlation. Both parameters are time-invariant and fixed during the inversion. We fix σ at
 42 ~ 0.02 based on the time-averaged standard errors obtained during the GF stacking. The
 43 temporal correlation r is associated with the low-pass filter by $r = e^{-(a\Delta t)^2}$, where a is a
 44 parameter of the low-pass filter and Δt is a waveform sampling interval.

45 For each iteration step, a new model is proposed by slightly modifying the current model. We
 46 allow five types of proposals: (1) adding a new layer interface; (2) removing a layer interface;
 47 and perturbing the (3) layer interface depth, (4) Vp anomaly, and (5) Vs anomaly. The amount
 48 of perturbation is randomly extracted from a normal distribution with a certain standard
 49 deviation (Table S2). After calculating the likelihood, the proposed model is accepted or
 50 rejected in accordance with the Metropolis-Hastings-Green criterion (Green, 1995).
 51 Irrespective of this criterion, we reject proposals of an anomalous layer with low Vp (< 0.1
 52 km/s), Vs (< 0.0 km/s) or Vp/Vs (< 1.5), or high Vp (> 8.6 km/s), Vs (> 5.0 km/s) or Vp/Vs (> 7.0).
 53 This additional condition may be regarded as another class of prior beyond the description of
 54 Equations S2–S5.

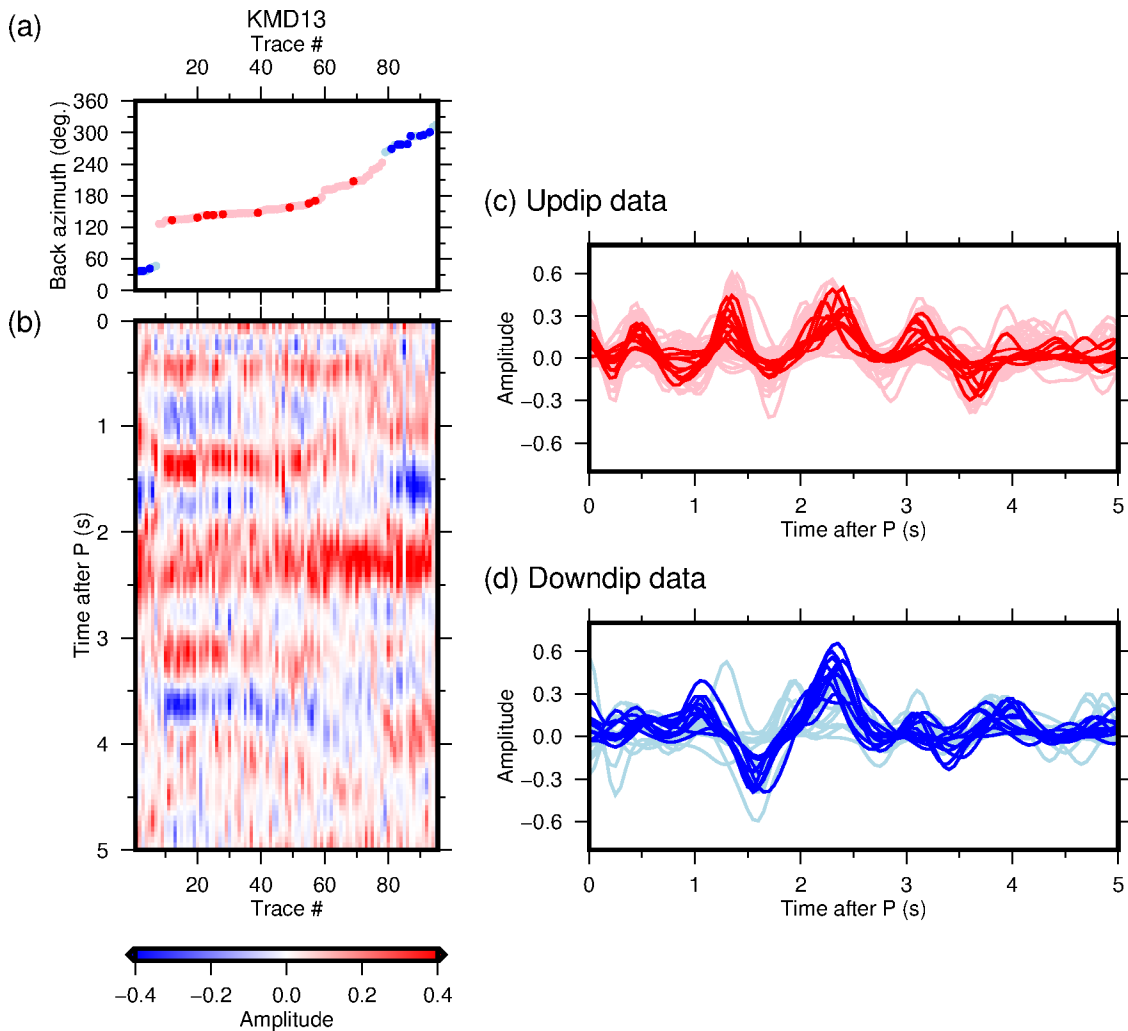
55 The aforementioned iteration is repeated 5×10^5 times; however models sampled during the
 56 first 2.5×10^5 iterations are not saved to eliminate initial sample dependency (termed the burn-
 57 in period). Even after the burn-in period, we only save the model once every 100 iterations to
 58 avoid artificial correlation with the previous samples. Furthermore, we employ the parallel
 59 tempering technique (Sambridge, 2014), in which 100 MCMC sampling processes run in
 60 parallel. Out of the 100 processes, 80 are tempered with different temperatures: The
 61 acceptance criterion is modified in response to the temperature such that higher temperature
 62 processes can more frequently accept proposals. The remaining 20 processes are given a unit
 63 temperature and used to estimate the posterior probability. At every iteration, the
 64 temperature may be swapped between processes, allowing a long jump in the model space.
 65 In this manner, we finally construct the posterior probability from a total of 5×10^4 models.

66

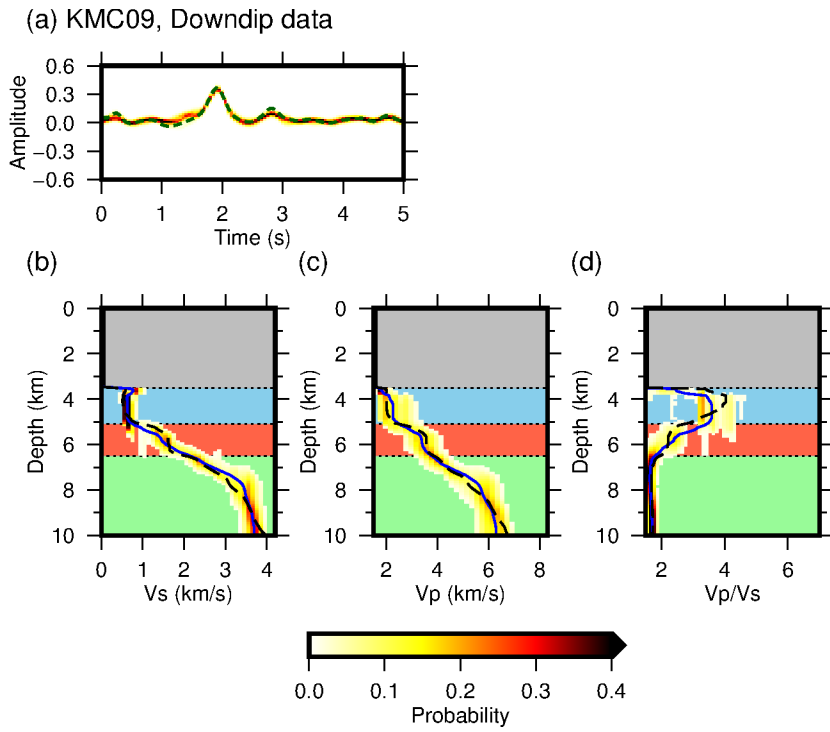
67



69
 73 **Figure S1.** P-wave velocity (V_p) models by previous studies. (a) The profile locations of the V_p
 74 models by Park et al. (2010) and Kamei et al. (2013), which are shown by the green and red
 75 lines, respectively. (b) The V_p model by Park et al. (2010). (c) The V_p model by Kamei et al.
 76 (2013). LVZ = low-velocity zone; PHS = Philippine Sea.
 74

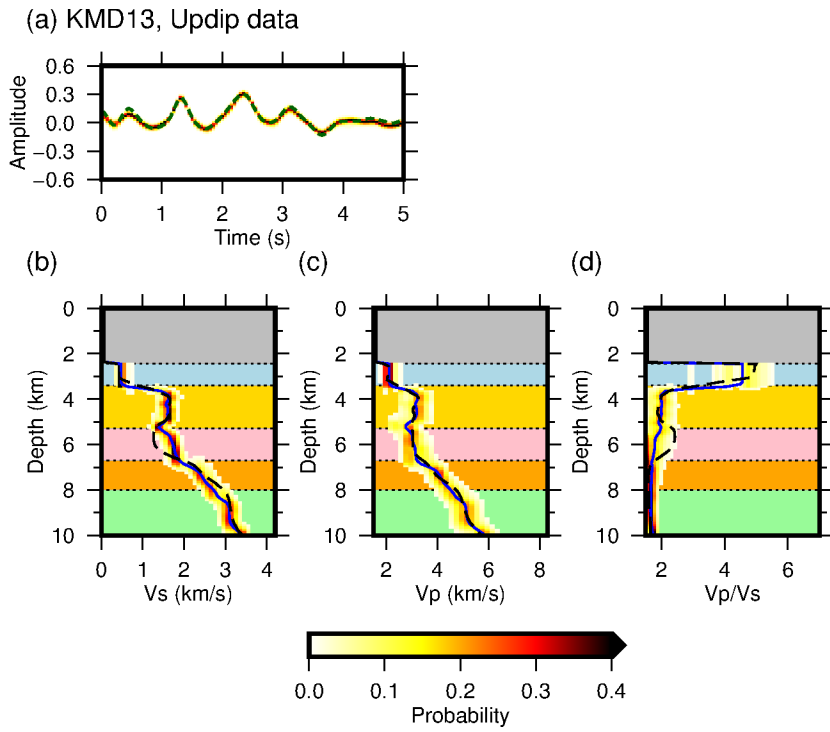


74
 75 **Figure S2.** Green's functions (GFs) calculated for KMD13. (a) Back azimuth of each GF shown in
 76 (b). Red and blue dots represent the updip and downdip data, respectively. Those selected for
 77 the inputs to the inversion analysis is shown in bright colors, while the others in pale colors. (b)
 78 GF amplitudes are shown in red (positive) and blue (negative) colors. (c-d) GFs included in (c)
 79 the updip and (d) downdip subsets. The color notation is the same as (a).



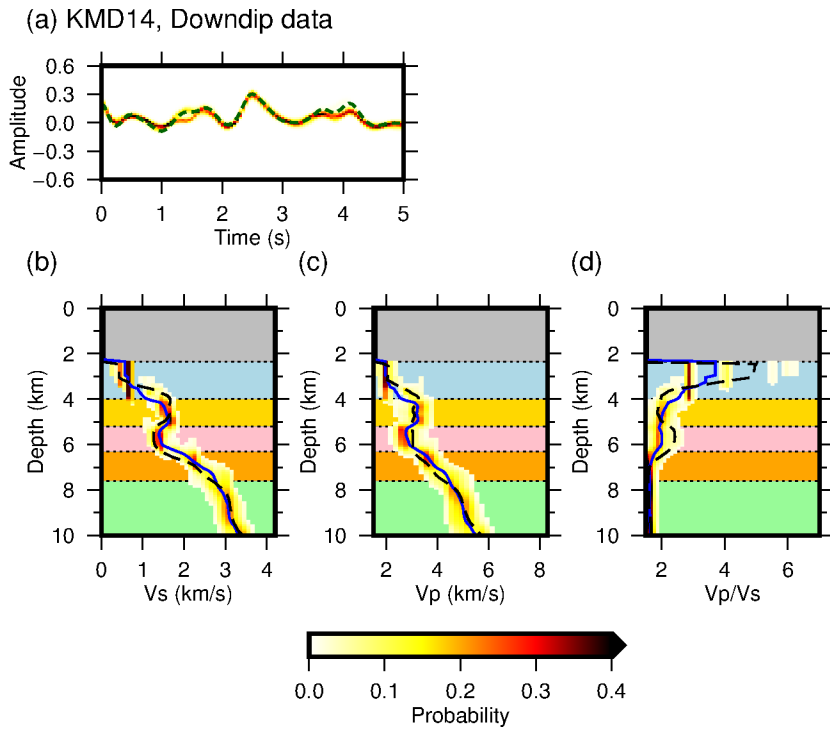
80
81
82
83
84
85

Figure S3. Results of inversion analysis for KMC09 with the downdip data. The notations are the same as Figure 2 in the main text except that the mean model from the updip data is shown by dashed lines for comparison.



86
87
88
89
90
91

Figure S4. Results of inversion analysis for KMD13 with the updip data. The notations are the same as Figure 2 in the main text except that the mean model from the downdip data is shown by dashed lines for comparison.



92
93
94
95
96

Figure S5. Results of inversion analysis for KMD14 with the downdip data. The notations are the same as Figure 2 in the main text except that the mean model from KMD13 (downdip data) is shown by dashed lines for comparison.

97 **Table S1.** Parameter choice for the prior probabilities.

Parameter	Value used in this study
k_{min}	1
k_{max}	21
z_{min}	Station level
z_{max}	10 km
$\sigma_{\delta\alpha}$	0.2 km/s
$\sigma_{\delta\beta}$	0.1 km/s

98

99 **Table S2.** Parameter choice for proposals.

Parameter	Value used in this study
Standard deviation for perturbing z_i	0.02 km
Standard deviation for perturbing $\delta\alpha_i$	0.03 km/s
Standard deviation for perturbing $\delta\beta_i$	0.03 km/s

100

101